HHS Public Access

Author manuscript

Eur J Neurosci. Author manuscript; available in PMC 2022 August 01.

Published in final edited form as:

Eur J Neurosci. 2021 August ; 54(4): 5357–5367. doi:10.1111/ejn.15335.

Gaze Mechanisms Enabling the Detection of Faint Stars in the Night Sky

Robert G. Alexander[1], **Ronald J. Mintz**[1], **Paul J. Custodio**[1], **Stephen L. Macknik**[1], **Alipasha Vaziri**[2,3,4], **Ashwin Venkatakrishnan**[1], **Sofya Gindina**[1], **Susana Martinez-Conde**[1,*]

[1]SUNY Downstate Health Sciences University, Brooklyn, NY, 11203, USA

[2]Laboratory of Neurotechnology and Biophysics, The Rockefeller University, New York, New York 10065, USA

[3]Kavli Neural Systems Institute, The Rockefeller University, New York, New York 10065, USA

[4]Research Institute of Molecular Pathology, 1030 Vienna, Austria

Abstract

For millennia, people have used “averted vision” to improve their detection of faint celestial objects, a technique first documented around 325 BCE. Yet, no studies have assessed gaze location during averted vision to determine what pattern best facilitates perception. Here, we characterized averted vision while recording eye-positions of dark-adapted human participants, for the first time. We simulated stars of apparent magnitudes 3.3 and 3.5, matching their brightness to Megrez (the dimmest star in the Big Dipper) and Tau Ceti. Participants indicated whether each star was visible from a series of fixation locations, providing a comprehensive map of detection performance in all directions. Contrary to prior predictions, maximum detection was first achieved at ~8° from the star, much closer to the fovea than expected from rod-cone distributions alone. These findings challenge the assumption of optimal detection at the rod density peak and provide the first systematic assessment of an age-old facet of human vision.

Graphical Abstract

*Corresponding Author and Lead Contact: S.M.C. (smart@neuralcorrelate.com).

Author Contributions

R.G.A., S.L.M., and S.M.C. conceptualized, planned, and supervised the project. R.G.A., S.L.M., Alipasha V., and S.M.C. contributed to the design and analysis. P.J.C. and Ashwin V. conducted formal analyses of the data. R.G.A., P.J.C., and S.G. contributed to data collection. R.G.A., R.J.M., and S.M.C. wrote the manuscript.

Data and Code Sharing Statement

Analyses are ongoing for additional hypotheses that are not included in the present study. Once such analyses are complete, the data that support the findings reported in this study will be available at doi:10.6084/m9.figshare.14668722

The authors declare no competing financial interests.

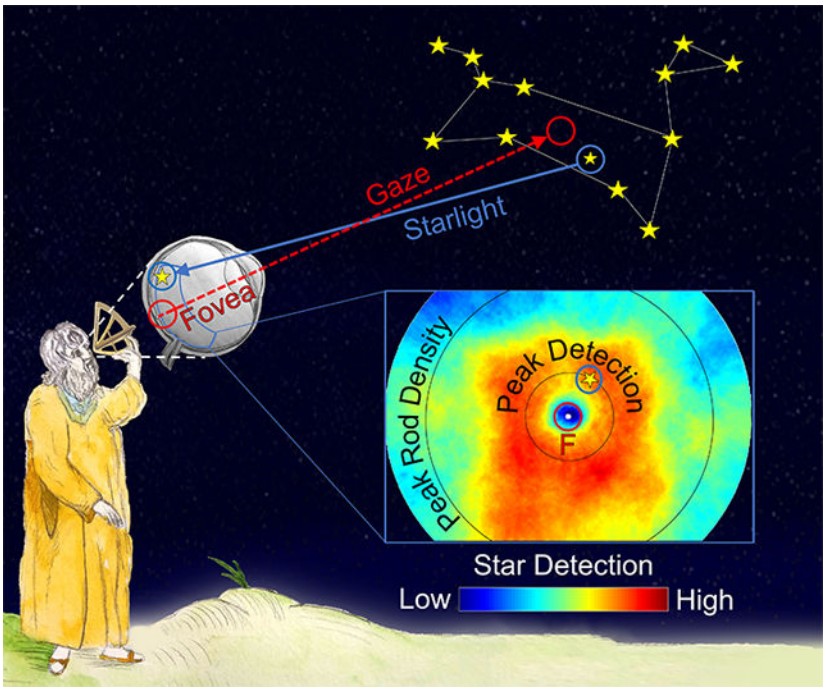

For over 2,000 years, stargazers have used “averted vision” to improve their detection of celestial objects. We tracked eye position during averted vision to determine the gaze patterns that produce optimal star detection, for the first time. Detectability was highest at ~8–14° from the star, contrary to prior predictions that peak star detection should overlap with the peak of retinal rod density.

Keywords

averted vision; dark adaptation; scotopic vision; eye movements; stargazing; fixation; gaze; eye tracking; rods; cones; peripheral vision; detection performance

Introduction

Human attention, eye movements, and perception are so tightly linked that we almost always attend to our gaze location—a relationship so consistent that deviations from it can be used to characterize neurological disease (Alexander, Macknik, & Martinez-Conde, 2018; Ciuffreda & Tannen, 1995; Subramanian, Jost, & Birch, 2013). Because our visual acuity is highest in the fovea, we usually attain the greatest amount of information about a stimulus by looking directly at it. Night vision, however, operates under different principles, due to being mediated by rods rather than cones. Because rods are absent from the fovea, looking directly at a stimulus is not the most adaptive way to gain information in the dark.

Around 325 BC, Aristotle wrote that gazing indirectly at one of the stars in the Great Dog constellation allows the viewer to see it more clearly than looking straight at it (Aristotle, 325 BCE). This indirect viewing technique, known as averted vision, has remained in use among stargazers for over 2,000 years, as a means to improve one’s naked-eye detection of faint celestial objects. The presumed reason for averted vision’s superiority in night-vision

conditions is that rod density is highest at an eccentricity of ~20°–25° of visual angle away from the fovea (20° temporal retina and 25° nasal retina (Wells-Gray et al., 2016)). Looking at a star from such an eccentricity should result in its light falling on the highest number of rods. However, no previous studies systematically assessed gaze location during averted vision. Thus, the above hypothesis and explanation have not been challenged.

Indeed, the precise viewing pattern that best facilitates perception during averted vision has never been ascertained, with different authors advising viewing distances ranging from 2° to 30° so as to maximize night-time detection (Astronomical Society of the Pacific, 2008; Azevedo & Mann, 2016; Barrett, 1977; Hallett, 1998; Miller & Tredici, 1992; Mobberley, 2009, p. 198). It follows that optimal star detection could be driven by a variety of factors, including a) rod density distribution, b) rod convergence with ganglion cells at different eccentricities, and c) neuronal densities in the downstream retinal circuit for rod photoreceptors, among others. The first two possibilities would predict peak star detection at ~20°–25° (Goodchild, Ghosh, & Martin, 1996; Riopelle & Chow, 1953), though the third one would do so at 2°–7° (Lee et al., 2019).

Here, we characterized averted vision while recording the eye positions of dark-adapted human participants with high precision, for the first time.

We used a CRT monitor in combination with various neutral density filters to create centrally-placed dim simulated stars of apparent magnitudes 3.3 and 3.5, which made their respective brightness equivalent to those of Megrez (Delta Ursae Majoris; the dimmest of the seven stars in the Big Dipper) and Tau Ceti (the second closest spectral class G star to the Sun, after Alpha Centauri A). After a dark-adaptation period, human participants made eye movements to a series of fixation targets at different positions on the screen and indicated whether the star was visible from each fixation location. This provided us with a comprehensive map of detection performance in all directions surrounding the star, up to 32.5° of horizontal eccentricity and 20.25° of vertical eccentricity from the star's position at the center of the screen.

If rod distribution was the sole predictor of performance, as previously assumed by most, peak detection should have occurred ~20°–25° away from the star. Contrary to this prediction, we found that participants first achieved peak detection performance at ~8° from the star; that is, much closer to the fovea than expected from photoreceptor distributions alone—or from rod convergence with ganglion cells. Instead, peak perceptual performance from averted vision may result from neuronal density in the downstream retinal circuit for rod photoreceptors (Lee, Martin, & Grünert, 2019) or from the delicate interplay between retinal eccentricity, photoreceptor density, and receptive field size.

These findings solve a historical perceptual puzzle, while challenging the assumption of optimal nighttime detection at the peak of the rod density distribution. Our conclusions have implications for patients suffering from night-vision disorders such nyctalopia (night blindness), as well as from conditions that impair central vision, such as macular degeneration.

Methods

Participants

Data were collected from 12 participants (8 naive; 8 female; 10 right-handed) in Experiment 1, and from 14 participants (8 naive; 9 female; 14 right-handed) in Experiment 2. All participants reported normal or corrected-to-normal vision. Data from 2 additional participants in Experiment 1 were collected but excluded from further analysis due to trial failure in >50% of the trials. Data from 2 additional participants in Experiment 2 were collected but excluded from analysis due to those participants achieving less than 75% accuracy at all distances. Participants received $15 for their participation and were debriefed after the experiments. The experiments were undertaken with the understanding and written consent of each subject, and the study conforms with the World Medical Association Declaration of Helsinki (2013). The procedures were carried out under the guidelines and approval of the SUNY Downstate Institutional Review Board (protocol number 690152).

Apparatus

Human participants rested their head on a chin rest. Gaze position was sampled at 500 Hz and recorded noninvasively in both eyes, using an EyeLink® 1000+ eye-tracker.

Three neutral density filters, made from tinted lucite of approximately −0.2, −0.6, and −1.1 log units, were placed in front of a linearized Barco CID 421 monitor. A frame was assembled around the filters such that no light from the monitor was visible except through the filters. This frame covered the bottom 1 cm of the screen, without affecting any of the visual stimuli presented. The monitor was set to a 1024×768 screen resolution and a 100 Hz refresh rate.

The horizontal range from the center of the display was 20.5° for Experiment 1 and 32.5° for Experiment 2; the vertical range was 15° for Experiment 1 and 20.25° for Experiment 2. To increase the horizontal and vertical ranges in Experiment 2, we decreased the distance between the monitor and the participant. Thus, the distance between the monitor and the participant was 53.0 cm in Experiment 1, and 31.5 cm in Experiment 2.

To allow for proper gaze calibration in Experiment 2, we placed a hot mirror (450 × 375 mm × 3.3 mm) between the monitor and the participant. The hot mirror was positioned at a 38° angle, such that the participant could see the monitor, and the infrared illumination from the eye tracker (now placed off to the side of the setup) reflected off the hot mirror to reach the participant’s eyes.

Star simulation

We created a simulated star by displaying a pixel-sized dot on the CRT monitor through the above-mentioned set of neutral-density filters, to reduce its brightness. Post-filtering, the simulated star’s resulting brightness was equivalent to that of a star of 3.3 apparent magnitude in Experiment 1, and a star of 3.5 apparent magnitude in Experiment 2 (Dufay & Gingerich, 2012), as per the calculations below. Correspondingly, the simulated star brightness was lower in Experiment 2 than in Experiment 1. Testing a dimmer simulated

star in Experiment 2 allowed us to gain insight into how changes in the brightness of a test stimulus might affect the dynamics of averted vision. We identified the astronomical magnitude of the simulated stars in both experiments in the following way:

We used a spectrometer (Ocean Optics USB 2000+) with a bare optical fiber (no attached lenses) to measure the spectral irradiance at each wavelength of the simulated star stimulus (without neutral density filters, at an arbitrary brightness selected during piloting). The spectrometer's software (OceanView 1.5.2, Ocean Optics) subtracted out background light from other detected sources, including the black background that surrounded the simulated star on the monitor. We then used a Gaussian filter to compute a weighted sum over the visible spectrum and to de-weight measurements towards the edge of the visual spectrum. Specifically, we used a Gaussian centered on 551 nm, with a full width half max of 88 nm and a maximum value of 1 (at the center of the Gaussian), to weight the spectral irradiance at each frequency (per nm) (Binney & Merrifield, 1998). Next, we computed the area under the curve of the weighted irradiance, to obtain the total irradiance of the simulated star (Binney & Merrifield, 1998).

We then calculated φ_H, the radiant flux through the pupil of a participant viewing the simulated star stimulus on the monitor. This was accomplished using the following equation to adjust for the difference in size between the recording surface from the spectrometer and the size of the human pupil, as well as for the difference in distances between the spectrometer and the stimulus during measurement, and between the participant and the stimulus during the experimental session (see Stimulus Generation section, below, for the derivation of this equation):

$$\varphi_H = (d_S/d_H)^2 E_S \pi r_H^2$$

Where d_S is the distance between the optical fiber of the spectrometer and the stimulus during the recording (1 cm), and d_H is the distance between participant and stimulus during the experimental session (53.0 cm for Experiment 1, and 31.5 cm for Experiment 2). E_S is acquired from the spectrometer recordings and denotes the irradiance (in microwatts per square centimeter) of light from the simulated star on the receiving area of the optical fiber of the spectrometer. Πr_H^2 is the area of the human pupil; we estimated r as 0.35 cm for the purpose of these calculations. We then adjusted for the fact that we would be using neutral density filters to reduce the irradiance during the actual experiments, by multiplying the radiant flux by $10^{-1.9}$.

To determine the apparent magnitude of a star which matched that radiant flux through the pupil, we entered the radiant flux (now converted to watts) into the following equation:

$$\left([\text{Lstar}/\text{Lsun}]/\text{lightyearsAway}^2\right) = 4 * \pi * \text{lightyear}^2 * \text{pupilPower}/(\text{pupilArea} * \text{sunPower})$$

We derived this equation by computing the proportion of the radiant flux of a star in all directions that passes through the participant's eye, multiplying the flux by the ratio of the area of the human pupil to the surface area of a sphere centered at the star.

Then, we determined the star magnitude by directly comparing the properties of the star stimulus ([Lstar/Lsun]/lightyearsAway^2) with the known properties of the Earth's Sun. Thus, to get the star magnitude, we used the following formula (Binney & Merrifield, 1998):

$$\text{StarMagnitude} = \text{SunMagnitude} - 2.5 * \log_{10}\left(\left([\text{Lstar/Lsun}]/[\text{lightyearsAwaySun/lightyearsAwayStar}]^2\right)\right)$$

Where the constant SunMagnitude is −26.73 and lightyearsAwaySUN is $1.58*10^{-5}$. The resulting values provided apparent magnitudes approximating those of real stars (Megrez—Delta Ursae Majoris in Experiment 1, and Tau Ceti in Experiment 2). Thus, the simulated stars displayed during the experiments had comparable perceptual brightness to that of observable stars in the night sky.

Stimulus Generation

The methods described here determine the R,G,B color values for a pixel on a CRT monitor, which (after filtering) equal the perceived brightness of a star that is faintly visible to the naked eye. This process requires finding a correspondence between suitable (R,G,B) values of screen pixel values, combined with an attenuation factor of filters applied to the display screen to reduce its brightness, and making irradiance measurements with a spectrometer. The output of this procedure is the apparent (i.e. astronomical) magnitude of the simulated star. The same sequence of steps can be followed with different pixel values and/or different filters to simulate stars of different apparent magnitudes. An intermediate quantity in the above calculation is the power (in microwatts) that the simulated star transmits through the pupil of the human eye, which we describe as follows.

Conversions, Computing Microwatts Entering the Pupil from Spectrometer Output, and Irradiance of the Star

We used an Ocean Optics USB 2000+ to produce spectral data containing the measurement of spectral irradiance from the center star on the computer screen at each wavelength in the visible spectrum, in units of microwatts per square centimeter per nanometer of wavelength (for the pixel brightness value being measured). We used the measurements of spectral irradiance output from the spectrometer to calculate the number of microwatts entering the human pupil, as a function of the spectral data and the filter attenuation factor. Because the Ocean Optics spectrometer was unable to provide reliable measurements of the light source with the neutral density filters in place, we did not use the neutral density filters when using the spectrometer, but multiplied the measured flux by the filter attenuation factor ($10^{-1.9}$, representing the combined effect of the three $10^{-0.2}$, $10^{-0.6}$, and $10^{-1.1}$ neutral density filters used during the experiments). We also adjusted for the ratio of the surface area where the pupil absorbs light energy to the corresponding available area for the spectrometer (the surface area of the bare filter). This conversion implements one of the mappings shown in Figure 1.

We computed the irradiance over the visual spectrum by taking a weighted sum of the spectral irradiance (per nm) at each of wavelengths in 400 to 700 nm spectrum multiplied by the width in nm for each value of spectral irradiance.

$$f(x) = e^{-b(x - x_0)^2} \quad (1)$$

Where the weighting factor f(x) for wavelength x is a Gaussian with maximum value 1 at x = x_0 (the midpoint for the wavelengths) and a specified value for the dispersion determined by the FWHM (full width half max). We used values of x_0 = 551 nm and FWHM = 88 nm to remove from consideration any irradiance beyond the visual spectrum. Parameter b, used in generating this Gaussian, is computed from FWHM by:

$$b = \frac{4 \ln 2}{FWHM^2} \quad (2)$$

We compute the irradiance over the visual spectrum of 400 to 700 nm as:

$$\sum_{i=1}^{nw-1} 0.5 * (m_i f(w_i) + m_{i+1} f(w_{i+1})) * (w_{i+1} - w_i) \quad (3)$$

Where:

w_i = wavelength i for 1 <= I <= nw

m_i = spectrometer measurement for wavelength i

m_i $f(w_i)$ = weighted spectrometer measurement for wavelength i

Radiant flux through the pupil:

Next, we computed the radiant flux through the human pupil from the simulated star.

The radiant intensity of a point light source, which we denote as L, is the radiant flux emitted per unit of solid angle along a cone of transmission from the source, here measured in microwatts per steradian. This quantity is dependent only on the light source, not on any receiving object. We therefore express L in terms of the spectrometer measurement E_S, and then use L to calculate φ_H, the radiant flux entering the human pupil.

Ω_S is the solid angle (in steradians) from the simulated star to the receiving area of the spectrometer.

Ω_H is the solid angle from the simulated star to the human pupil.

φ_S is the radiant flux (in microwatts) from the simulated star that enters the receiving area of the spectrometer.

φ_H is the radiant flux (in microwatts) from the simulated star that enters the human pupil.

A_S is the surface area (in square centimeters) of the receiving area of the spectrometer.

A_H is the surface area (in square centimeters) of the human pupil, which is πr_H^2, where r_H is the human pupil radius.

d_S is the distance (in centimeters) from the simulated star to the receiving area of the spectrometer.

d_H is the distance (in centimeters) from the simulated star to the human pupil.

E_S is the irradiance (in microwatts per square centimeter) of light from the simulated star on the receiving area of the spectrometer.

Before deriving an expression for φ_H in terms of E_S, we need to derive a simple expression relating surface area to solid angle. The surface area of a sphere of radius r is $4\pi r^2$. The solid angle circumscribed by a complete sphere is 4π. Letting A be the surface area of the part of a sphere with radius r cut off by a cone with solid angle Ω,

$$\mathbf{A} = 4\pi r^2(\Omega/4\pi \text{ steradians}) = \boldsymbol{\Omega r^2}. \quad (4)$$

By definition, $L = \varphi_S / \Omega_S$, the radiant flux emitted per unit of solid angle, and $\varphi_S = E_S A_S$, the irradiance multiplied by the surface area. Therefore, $L = E_S(A_S/\Omega_S)$.

From equation (4), $A_S = \Omega_S d_S^2$, since d_S is the radius of the sphere centered at the simulated star and including the receiving area of the spectrometer's bare fiber. Thus, $L = E_S d_S^2$, expressing L in terms of the spectrometer measurement E_S.

We now express φ_H, the radiant flux entering the human pupil, in terms of L. $\varphi_H = L \Omega_H$ by the definition of L. From equation (4), the solid angle from the simulated star to the human pupil $\Omega_H = A_H / d_H^2$. Therefore $\varphi_H = L A_H / d_H^2 = E_S A_H (d_S^2 / d_H^2)$. Since $A_H = \pi r_H^2$, we get the result $\boldsymbol{\varphi_H = (d_S/d_H)^2 E_S \pi r_H^2}$ (the first equation in the main text of the manuscript). Since filters were added for the experiments with human participants, but not for the spectrometer measurements, the resulting radiant flux value φ_H is multiplied by the factor $10^{0.1 * \text{filter}}$.

Procedure

Participants dark-adapted their vision by sitting in a completely dark room for 20 minutes. We then calibrated the eye tracker and began the experimental sequence. Participants fixated a target (a 0.2° black circle within a 0.4° gray circle) that was displayed on different positions on the monitor and made a yes/no judgment (via button-presses) about the presence of a central simulated star (after foveating the fixation target). The fixation target was presented pseudorandomly across the display, such that it never appeared within 0.5° of the center of the display or within five degrees of the previous fixation target location. The angle around the center of the display and the distance from the center were approximately uniformly distributed, over 0°– 360° and over 0.5°–20.5°, respectively. If a selected location was outside the display's vertical range (15° from center for Experiment 1 and 20.25° from center for Experiment 2), a new location was selected. The simulated star was present on the

display 50% of the time, and always appeared in the center of the display so that participants could easily locate its position (using the always-visible edges of the monitor as a reference).

To ensure that participants' responses were driven by detection of the star, rather than by transients caused by the star's appearance or disappearance, we updated the computer display to display or remove the star while the participants shifted their gaze towards each subsequent fixation target location. Because humans are typically unaware of visual changes that occur during saccades (Bridgeman & Macknik, 1995; Macknik, Fisher, & Bridgeman, 1991), this procedure minimized the possibility that participants would notice (or respond to) transients caused by changes in the display (see (Alexander, Schmidt, & Zelinsky, 2014; Grimes, 1996) for similar approaches). We also conducted a pilot version of the present experiment, which updated the screen during the subjects' instructed blinking (rather than during a detected saccade). The results from the pilot study were similar to those reported here.

At each fixation target location, participants indicated whether the star was present or absent by pressing the right vs. left trigger buttons of a Gamepad controller. Trials were aborted (trial failure) if participants did not look at the fixation target within 1.5° of the fixation target's center within 3 seconds of its appearance on the display, if they failed to respond within 3 seconds of fixating the target, or if they looked more than 1.5° away from the fixation target for more than 0.5 seconds before providing a response. In such cases, a new fixation target was presented, and a "time-out" error was recorded. See Figure 2 for a schematic representation of the procedure. Trials were presented in 2-minute blocks and participants manually initiated the next block of trials at the end of each block. Experiment 1 was conducted in a single session and included 10 experimental blocks, amounting to 27.5 minutes total (652.4±43.6 trials per subject). Experiment 2 was conducted in two sessions, each including 10 experimental blocks (1158.1±67.8 trials per subject).

Data Analysis

To examine the patterns of detection performance as a function of gaze direction and distance from the star, we created heatmaps representing the accuracy at each fixation location across participants. These heatmaps only included trials where participants gazed at the fixation target and subsequently provided a yes/no response. Individual heatmaps were created from the button-press responses (coded as zero for incorrect responses and 1 for correct responses) that each participant produced. Each pixel of the heatmap was given a value between 0 and 1, calculated from an inverse distance weighted average of responses for the nearest 20 fixation targets to that pixel (assigning linearly decreasing weights with increasing ordinal rank distance). Thus, button-press responses produced while gazing nearer to a pixel on the heatmap were given a higher weight than button-press responses made while gazing farther away. Each pixel on the heatmap therefore represents performance accuracy near that region of the display. Average heatmaps were created by averaging the values of each corresponding pixel location across the heatmaps of individual participants. We used Wilcoxon signed rank tests for all statistical comparisons, except where otherwise noted. To minimize the likelihood of type II error, we assumed statistical significance only for values of $p < .05$.

Results

Experiment 1

Human participants made eye movements to a series of fixation targets after dark-adapting for 20 minutes. At each fixation location, subjects made a yes/no judgment about whether a simulated central star was displayed on the center of a computer screen subtending 20.5° (h) × 15° (v). This simulated star had an apparent magnitude of 3.3 (an equivalent brightness to Megrez, the dimmest star in the Big Dipper).

Detection accuracy was lowest from fixation locations within 1° of the star and highest from fixation locations ~8° from the star. For fixation locations nearest to the star, detection accuracy was reduced to chance levels (z=0.94, p=.3476). This was an expected finding, given that the center of the human retina is devoid of rods (Curcio, Sloan, Kalina, & Hendrickson, 1990; Osterberg, 1935), but nevertheless valuable in that it demonstrated that the simulated star was dim enough to be detectable only through averted vision (and not when foveated) under scotopic conditions. These data further supported the ecological validity of the visual stimulation parameters chosen to display the simulated star, as dark adaptation combined with the presence of a small, faint visual object results in the conditions where averted vision is perceptually advantageous.

Importantly, if solely determined by rod-cone distribution, performance should have peaked at an eccentricity of ~20°–25°. Contrary to this prediction, we found that maximum detection accuracy was first achieved at ~8° from the star (Figure 3). Performance in the 8°–14° range was significantly higher than 84.7% (i.e. the average accuracy across all distances), z=8.37, p=5*10^{-17}, and decreased at greater eccentricities. Performance in the 19.5°–20.5° range was significantly lower than in the 8°–14° range (W=−60, p=.0161), but did not significantly differ from the average accuracy across all distances, z=0.49, p=0.6218. See Supplemental Figure 1A for individual participant results.

Naive (Supplemental Figure 1B) and non-naive (Supplemental Figure 1C) participants displayed comparable performance patterns: both participant groups performed at chance within 1° of the star stimulus, reached peak performance in the 8°–14° range, and showed decreased performance at eccentricities greater than 14°.

The accuracy heatmap (Figure 4) showed that maximum performance in the 8°–14° range extended in all directions around the compass, without revealing any particularly ineffective areas in the visual field for averted vision—aside from the regions of minimal sensitivity near the center of the display, and at the furthest (horizontal) eccentricities. Likewise, there were no particularly effective areas in the visual field outside of the above mentioned 8°–14° eccentricity range. Star locations estimated as falling on either optic disc did not result in reduced performance when compared to other equidistant locations. This was anticipated because participants performed the task binocularly.

Experiment 2

Experiment 1 showed that maximum performance occurred nearer the star stimulus than predicted by rod-cone distribution alone (i.e. as close as ~8°, rather than at 20°–25°), but

it did not establish whether accuracy reached a plateau at ~15°, or decreased even more at further eccentricities.

Thus, Experiment 2 extended the eccentricities tested from 20.5° to 32.5° in the horizontal range, and from 15° to 20.25° in the vertical range. We also displayed a dimmer star to ascertain if the 8°–14° peak in performance was idiosyncratic to the specific stimulus presented in Experiment 1, or robust to a variety of perceived brightness values of the star stimulus. This new simulated star had an apparent magnitude of 3.5 (an equivalent brightness to Tau Ceti).

Consistent with the results from Experiment 1, we found chance levels of performance (43.0±4%) at eccentricities in close distance to the simulated star (0.5°–1°)—z=−1.59, p=.1123—see Figure 5. Also in line with Experiment 1, we observed a steep rise in accuracy as eccentricity increased beyond the fovea, in addition to peak performance as close as ~8° from the star, despite having used stars with different brightness values in the two experiments. Once more, performance in the 8°–14° range was significantly higher than the average accuracy across all distances (74.6% average), z=10.8, p<0.0001. Performance in the 19.5°–20.5° range was again significantly lower than in the 8°–14° range, W=−105, p=.00012).

Beyond 15°, performance declined as a function of eccentricity, nearing chance levels at the farthest eccentricities tested. Thus, at eccentricities of 31.5°–32.5°, accuracy was close (i.e. statistically equivalent) to chance at 58.2±4% (z=1.99, p=.0471). In sum, Experiment 2's results provided additional evidence that averted vision performance peaks at ~8°–14°, followed by a steady decrease in performance with increasing eccentricities, approaching chance levels around ~30°. See Supplemental Figure 2A for individual participant results.

As in Experiment 1, performance was similar across naive (Supplemental Figure 2A), and non-naive participants (Supplemental Figure 2B).

Discussion

Averted vision is a viewing technique which entails looking away from an object in order to improve its visibility and detection. Though first described more than 2,000 years ago, instruction in averted vision has endured in modern military scenarios (Dyer & Mittelman, 1998; Liljencrantz, Swanson, & Carson, 1942; Military Intelligence Service, 1943; Rostenberg, 1944; Spicer, 2016; Sutherland, 2010) and remains relevant in contemporary astronomy, even when using a telescope (i.e. so as to place a faint celestial object on a more sensitive part of the observer's retina, within the telescope's field of view (Azevedo & Mann, 2016, p. 588; Coe, 2016; Cudnik, 2012)). Despite the long-documented history and running use of this method, no previous research has systematically assessed gaze location during averted vision to establish the pattern of viewing that best facilitates perception. Here, we set out to establish such a pattern via high-resolution eye-tracking and the presentation of simulated stars of comparable parameters to those of stars that are typically viewed via averted vision in the night sky, under dark adaptation conditions.

Tests of dark-adapted sensitivity have reported peak sensitivities up to the 20°–30° range (Crozier & Holway, 1939; Jackson & Owsley, 2000; Pulos, 1989; Riopelle & Bevan, 1953; Scholtes & Bouman, 1977; Sloan, 1947; Ten Doesschate, 1949). This prior work required participants to foveate locations at different eccentricities, but gaze was not monitored. It is therefore possible that participants unintentionally made small saccades towards the stimuli they were meant to discriminate, or allowed their gaze to drift in that direction, causing peak performance eccentricities to be overestimated. It follows that unexplained discrepancies in sensitivity across studies might be at least partly due to differences in participants' compliance. In contrast, our use of eye-tracking allowed for the measurement and enforcement of participants' gaze position in the present experiments.

Optimal eccentricity for perception during averted vision

If improved perception during averted vision results from light falling on retinal areas where rod density is highest, then detection should be optimized at ~ 20°–25° from the star—the known peak of the rod density distribution in human vision (Curcio et al., 1990; Osterberg, 1935). However, the pattern could be more complex than a linear improvement in performance as gaze approaches an eccentricity of 20°. Indeed, different sources recommend viewing faint stellar phenomena at wide-ranging distances so as to maximize detection, from near central vision to as far in the periphery as 30°, with the strongest claims made for eccentricities in the 20° range. Among these distances are 2° (Barrett, 1977), 8°–16° (Azevedo & Mann, 2016; Mobberley, 2009, p. 198; Riopelle & Chow, 1953), and 15°–20° from the fovea (Astronomical Society of the Pacific, 2008; Miller & Tredici, 1992). In addition, various tests of dark-adapted vision have reported peak sensitivities in eccentricities ranging from 8° to 30° (Crozier & Holway, 1939; Pulos, 1989; Riopelle & Bevan, 1953; Scholtes & Bouman, 1977; Sloan, 1947; Ten Doesschate, 1949). Most of these distances cannot be explained by rod-cone distribution alone.

Some researchers proposed that the shape of the scotopic sensitivity curve could be partly driven by differences in rod coupling and convergence with bipolar and ganglion cells at different eccentricities (Crozier & Holway, 1939). However, later counts of the number of rods converging with ganglion cells found peaks of convergence around 20–25° (i.e. in the same eccentricity range as the peak of the rod-cone distribution) (Goodchild, Ghosh, & Martin, 1996; Riopelle & Chow, 1953). Thus, whether the sensitivity curve is driven by rod density and/or by convergence with ganglion cells, one would expect peak performance to occur in the 20–25° range.

More recent work has examined neuronal densities in the downstream retinal circuit for rod photoreceptors. In one study (Lee et al., 2019), rod bipolar cell density peaked at 7°–15°, and All-amacrine cell density did so at 2°–7°. These two densities combined could support peak averted vision performance in the 2°–15° range.

Contrary to most predictions and prior findings (but see (Jackson & Owsley, 2000; Riopelle & Chow, 1953; Scholtes & Bouman, 1977)), peak star detection did not take place in the 20–25° range in the present experiments, but instead occurred much closer to the star, at ~8°–14° (Figure 6). Thus, our results indicate that rod density is not the primary factor determining heightened performance in averted vision. Incidentally, the 8°–14° range

corresponding to peak performance in the present experiments coincides with the 8°–16° range reported by a few astronomers using averted vision in the field (Azevedo & Mann, 2016; Mobberley, 2009, p. 198).

We moreover note that, though some prior research suggested the possible presence of substantial individual differences in the direction and/or foveal distance of peak performance during averted vision (Mobberley, 2009; Ten Doesschate, 1949), we found that the pattern of detection performance held across participants, both individually and as a group, with little evidence of idiosyncratic variation as to the viewing distances resulting in the most accurate performance. Likewise, the two different star brightness values that we tested (in Experiment 1 and Experiment 2) had a negligible effect on the results observed.

Peak performance versus peak rod density

The explanation for why an eccentricity of ~8°–14° might result in peak detection performance during averted vision may reside in a combination of anatomical and physiological factors: though rod density increases with distance from the fovea (Wells-Gray et al., 2016), rod cells also increase in size linearly with eccentricity (Curcio, Millican, Allen, & Kalina, 1993). Larger photoreceptors have larger receptive field sizes (Snyder, 1975), and therefore lower spatial resolution. It follows that visual discrimination in scotopic conditions might be determined by the combination of rod density and receptive field size at any given eccentricity. Previous research also indicates that the optimal eccentricity for visual performance depends on the specific stimuli used, with higher detectability of larger stimuli at larger eccentricities than those of small stimuli (Scholtes & Bouman, 1977). Thus, eccentricities in the 8°–14° range may provide an optimal balance between rod density and rod size when star-gazing for small phenomena in dim light, despite departing from the 20°–25° range predicted by the prevalent claim that rod density alone is responsible the benefits of averted vision.

As previously stated, peak densities of neurons in the downstream circuit for rod photoreceptors moreover occur closer to the fovea than the peak rod density (2°–7° for All-amacrine cells and 7°–15° for rod bipolar cells (Lee et al., 2019). Thus, the density of these downstream neurons, rather than that of rods themselves, could help explain our findings.

Additionally, eccentricities closer to the fovea may draw greater benefits from perceptual training than more distant eccentricities, given that we usually look directly at the visual features we want to discriminate. Even when viewing larger objects or patterns, in which features of interest extend into the parafovea or further eccentric distances, relevant information does not commonly extend into the 20°–25° range. Thus, discrimination of relevant features takes place primarily in our central vision. Because improvements in the detection or discrimination of visual stimuli are usually limited to a particular retinal location (Ball & Sekular, 1987; Fahle, 2005) or even to the eye that is trained (Karni & Sagi, 1991), it could be that perceptual learning is more helpful at closer than at farther eccentricities—potentially improving performance in the 8°–14° range more than in the 20°–25° range.

Finally, it is worth noting that, though the present study displayed a single isolated star on a black background, there are additional reasons why eccentricities in the 20°–25° range are likely linked to worse detection of celestial objects in the field, compared to eccentricities in the 8°–14° range. Namely, the smaller receptive fields associated to the closer eccentricities are less liable to capture light from multiple celestial objects in the night sky. In contrast, larger receptive fields may average light from different sources, and in turn make double stars appear as single stars, faint stars less detectable when near bright objects, or distant galaxies washed out by the light from a single bright star.

Conclusions

Averted vision is a time-tested and valued means of improving one's perceptual performance in scotopic (i.e. night vision) conditions. Here we show that rod photoreceptor density, which is habitually invoked to explain enhanced detection during averted vision, does not fully account for heightened performance during stargazing. The current findings thus resolve a longstanding dispute, while providing the first perceptual and oculomotor assessment of an age-old facet of human visual experience. In addition, our results expand current understanding of visual discrimination outside the fovea, and may help elucidate the role of extrafoveal vision, not only in the healthy visual system, but also in ophthalmic conditions entailing night blindness (such as in retinitis pigmentosa) or the irreversible loss of central vision (such as in age-related macular degeneration).

Supplementary Material

Refer to Web version on PubMed Central for supplementary material.

Acknowledgments

This work was supported by the State of New York's Empire Innovator Program, the National Science Foundation (Award 1734887 to SMC and SLM), and the National Institute of Health (Award R01EY031971 to SMC and SLM; Award R01CA258021 to SMC and SM). We are indebted to Dr. Jonathan Victor for his loan of the neutral density filters used during these experiments. We thank Hannah Rosch-Newton for her help with data collection and Dr. Matthew Schneps, Dr. Michael Kurtz, and Dr. Nicolas Brunet for helpful discussions.

References

Alexander RG, Macknik SL, & Martinez-Conde S (2018). Microsaccade Characteristics in Neurological and Ophthalmic Disease. Front Neurol, 9(144), 1–9. doi:10.3389/fneur.2018.00144 [PubMed: 29403429]

Alexander RG, Schmidt J, & Zelinsky GJ (2014). Are summary statistics enough? Evidence for the importance of shape in guiding visual search. Visual Cognition, 22(3–4), 595–609. doi:10.1080/13506285.2014.890989 [PubMed: 26180505]

Aristotle. (325 BCE). Meteorology. Book I: Chapter 6: Alex Catalogue; NetLibrary.

Astronomical Society of the Pacific. (2008). Ready to Observe? How to Enhance Your Visitors' Experience at the Telescope. Night Sky Network Outreach Resources. Retrieved from https://nightsky.jpl.nasa.gov/docs/TTKReadyObserve.pdf

Azevedo FS, & Mann MJ (2016). Embodied Cognition in Observational Amateur Astronomy: Singapore: International Society of the Learning Sciences.

Ball K, & Sekular R (1987). Direction-specific improvement in motion discrimination. Vision Research, 27, 935–965.

Barrett A (1977). Notes-Aristotle and Averted Vision. Journal of the Royal Astronomical Society of Canada, 71, 327.

Binney J, & Merrifield M (1998). Galactic astronomy (Vol. 9): Princeton University Press.

Bridgeman BB, & Macknik SL (1995). Saccadic suppression relies on luminance information. Psychological Research, 58, 163–168. [PubMed: 8570784]

Ciuffreda KJ, & Tannen B (1995). Eye movement basics for the clinician. St. Louis: Mosby-Year book, Inc.

Coe SR (2016). What Are All These Different Types of Nebulae, and What Details Can I See in Them with My Telescope? Deep Sky Observing (pp. 133–177): Springer.

Crozier W, & Holway A (1939). Theory and measurement of visual mechanisms: I. A visual discriminometer. II. Threshold stimulus intensity and retinal position. The Journal of general physiology, 22(3), 341. [PubMed: 19873107]

Cudnik B (2012). Faint Objects and How to Observe Them: Springer Science & Business Media.

Curcio CA, Millican CL, Allen KA, & Kalina RE (1993). Aging of the human photoreceptor mosaic: evidence for selective vulnerability of rods in central retina. Investigative Ophthalmology & Visual Science, 34(12), 3278–3296. [PubMed: 8225863]

Curcio CA, Sloan KR, Kalina RE, & Hendrickson AE (1990). Human photoreceptor topography. J Comp Neurol, 292(4), 497–523. doi:10.1002/cne.902920402 [PubMed: 2324310]

Dufay J, & Gingerich O (2012). Introduction to astrophysics: the stars: Courier Corporation.

Dyer JL, & Mittelman MH (1998). Evaluation of an unaided night vision instructional program for ground forces. Military Psychology, 10(3), 159–172.

Fahle M (2005). Perceptual learning: specificity versus generalization. Curr Opin Neurobiol, 15(2), 154–160. doi:S0959–4388(05)00042–5 [pii] 10.1016/j.conb.2005.03.010 [PubMed: 15831396]

Goodchild AK, Ghosh KK, & Martin PR (1996). Comparison of photoreceptor spatial density and ganglion cell morphology in the retina of human, macaque monkey, cat, and the marmoset Callithrix jacchus. Journal of Comparative Neurology, 366(1), 55–75. doi:doi:10.1002/(SICI)1096-9861(19960226)366:1<55::AID-CNE5>3.0.CO;2-J

Grimes J (1996). On the failure to detect changes in scenes across saccades. In Atkins K (Ed.), Perception: Vancouver studies in cogntive science (pp. 89–110). New York: Oxford University Press.

Hallett PE (1998). Human Nocturnal Spectral Sensitivity and Photoelectric V. Journal of the American Association of Variable Star Observers (JAAVSO), 26, 139–150.

Jackson GR, & Owsley C (2000). Scotopic sensitivity during adulthood. Vision Research, 40(18), 2467–2473. [PubMed: 10915886]

Karni A, & Sagi D (1991). Where practic makes perfect in texture discrimination: Evidence for primary visual cortex plasticity. Proc. Natl. Acad. Sci, 88, 4966–4970. [PubMed: 2052578]

Lee SCS, Martin PR, & Grünert U (2019). Topography of Neurons in the Rod Pathway of Human Retina. Investigative Ophthalmology & Visual Science, 60(8), 2848–2859. [PubMed: 31260035]

Liljencrantz E, Swanson CA, & Carson LD (1942). The Use of the Eyes at Night (Vol. 68). United States Naval Institute Proceedings.

Macknik SL, Fisher BD, & Bridgeman B (1991). Flicker distorts visual space constancy. Vision Research, 31(12), 2057–2064. [PubMed: 1771791]

Military Intelligence Service. (1943). How to Use Your Eyes at Night. Intelligence Bulletin, 1(6).

Miller RE, & Tredici TJ (1992). Night vision manual for the flight surgeon. Retrieved from

Mobberley M (2009). Cataclysmic cosmic events and how to observe them: Springer Science & Business Media.

Osterberg G (1935). Topography of the layer of rods and cones in the human retina. Acta Ophthalmol, 13, 6–97.

Pulos E (1989). Changes in rod sensitivity through adulthood. Investigative Ophthalmology & Visual Science, 30(8), 1738–1742. [PubMed: 2759789]

Riopelle AJ, & Bevan W (1953). The distribution of scotopic sensitivity in human vision. The American journal of psychology, 66(1), 73–80. [PubMed: 13030848]

Riopelle AJ, & Chow KL (1953). Scotopic area-intensity relations at various retinal locations. Journal of Experimental Psychology, 46(5), 314–318. doi:10.1037/h0060283 [PubMed: 13109132]

Rostenberg L (1944). Combat importance of night vision training. Military Review.

Scholtes AMW, & Bouman MA (1977). Psychophysical experiments on spatial summation at threshold level of the human peripheral retina. Vision Research, 17(7), 867–873. doi:10.1016/0042-6989(77)90131-6 [PubMed: 898693]

Sloan LL (1947). Rate of dark adaptation and regional threshold gradient of the dark-adapted eye: Physiologic and clinical studies. American Journal of Ophthalmology, 30(6), 705–720. [PubMed: 20241735]

Snyder AW (1975). Photoreceptor optics—theoretical principles Photoreceptor optics (pp. 38–55): Springer.

Spicer M (2016). Illustrated manual of sniper skills: Pen and Sword.

Subramanian V, Jost RM, & Birch EE (2013). A Quantitative Study of Fixation Stability in AmblyopiaFixation Stability in Amblyopia. Investigative Ophthalmology & Visual Science, 54(3), 1998–2003. [PubMed: 23372053]

Sutherland D-M (2010). Identification of Soldier Behaviors Associated with Search and Target Acquisition (STA). Retrieved from

Ten Doesschate J (1949). Extra-foveal scotopic absolute threshold and the distribution of retinal rods. Ophthalmologica, 117(2), 110–115. [PubMed: 18115696]

Wells-Gray EM, Choi SS, Bries A, & Doble N (2016). Variation in rod and cone density from the fovea to the mid-periphery in healthy human retinas using adaptive optics scanning laser ophthalmoscopy. Eye, 30(8), 1135–1143. doi:10.1038/eye.2016.107 [PubMed: 27229708]

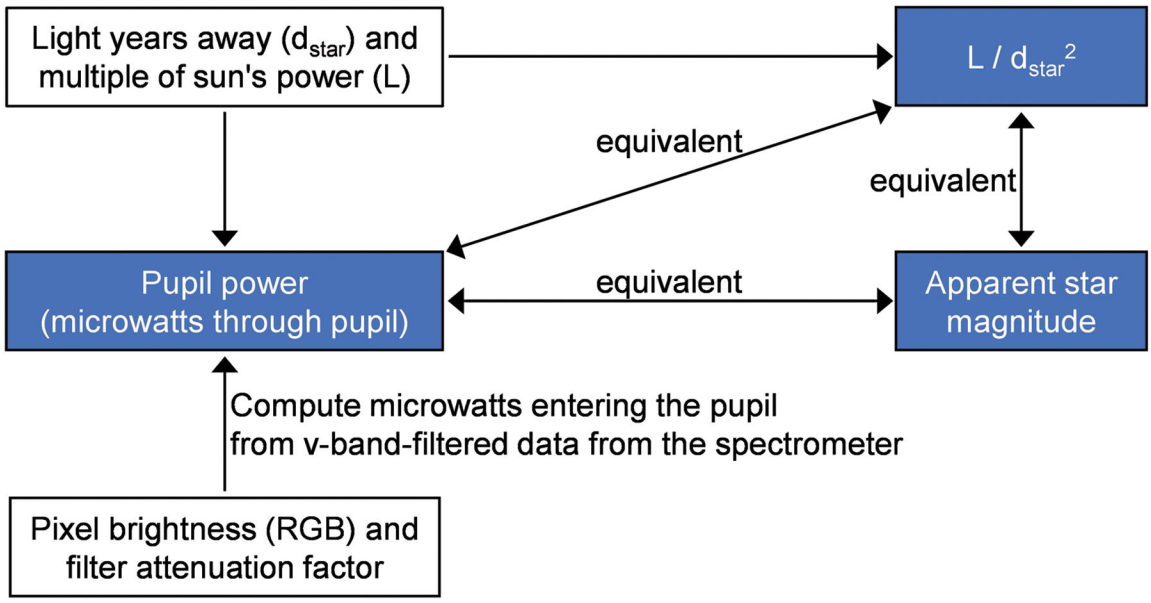

Figure 1.

The values and functions involved in the calculation of the pixel brightness used to simulate a star of a given apparent magnitude (or conversely, the values and functions involved in the calculation of the apparent magnitude of a given pixel). The calculations described in the Methods section were conducted to achieve equivalence between the three values denoted by the blue boxes in this figure.

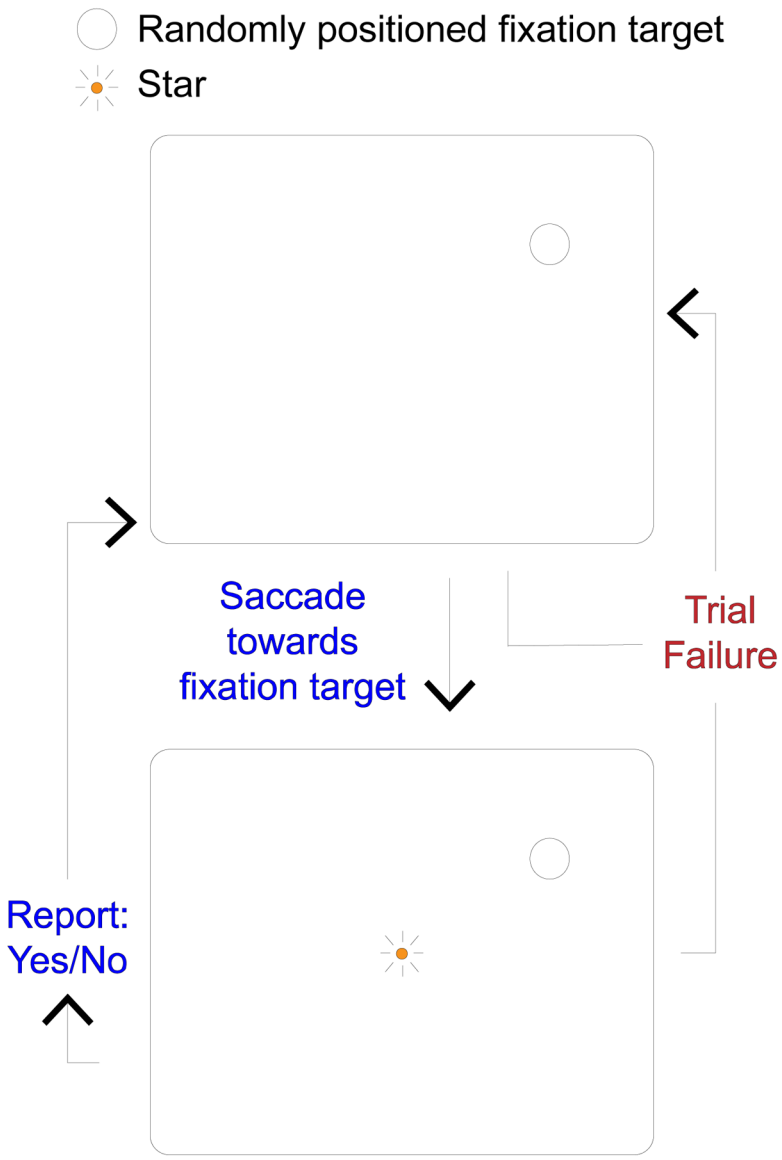

Figure 2.

Experimental design. Each block was participant-initiated. Participants were required to foveate the fixation target before making a yes/no response. Trials aborted if participants looked away from the fixation target before providing a response, if they failed to respond within 3 seconds of fixating the target, or if they did not look at the fixation target within 3 seconds of its appearance on the display.

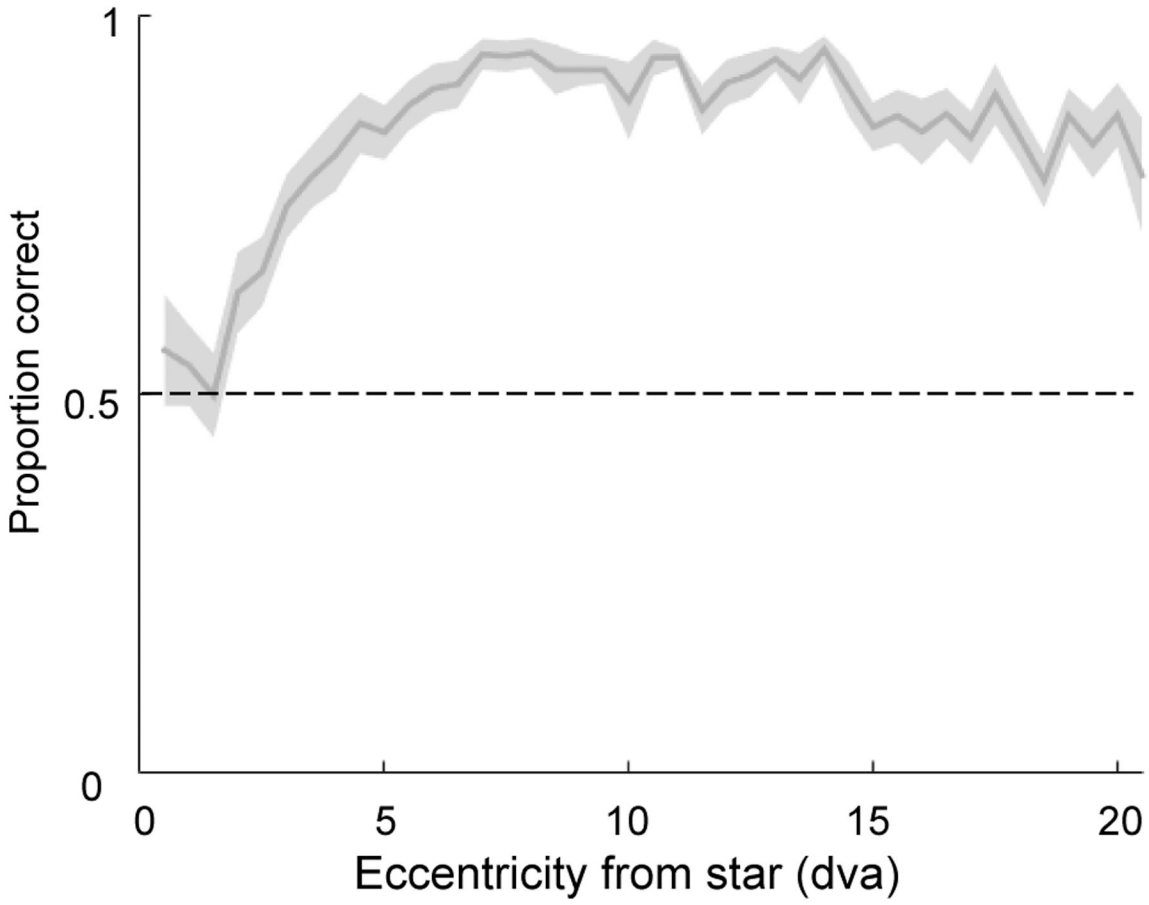

Figure 3.

Participants reached peak detection accuracy at lower eccentricities than predicted based on rod-cone distribution. Accuracy was characterized by chance levels of performance at the fovea, followed by a steep increase in performance peaking at ~8°, with a slow decline at eccentricities greater than 14°. Shading indicates SE. The dashed horizontal line indicates chance. N=12 participants.

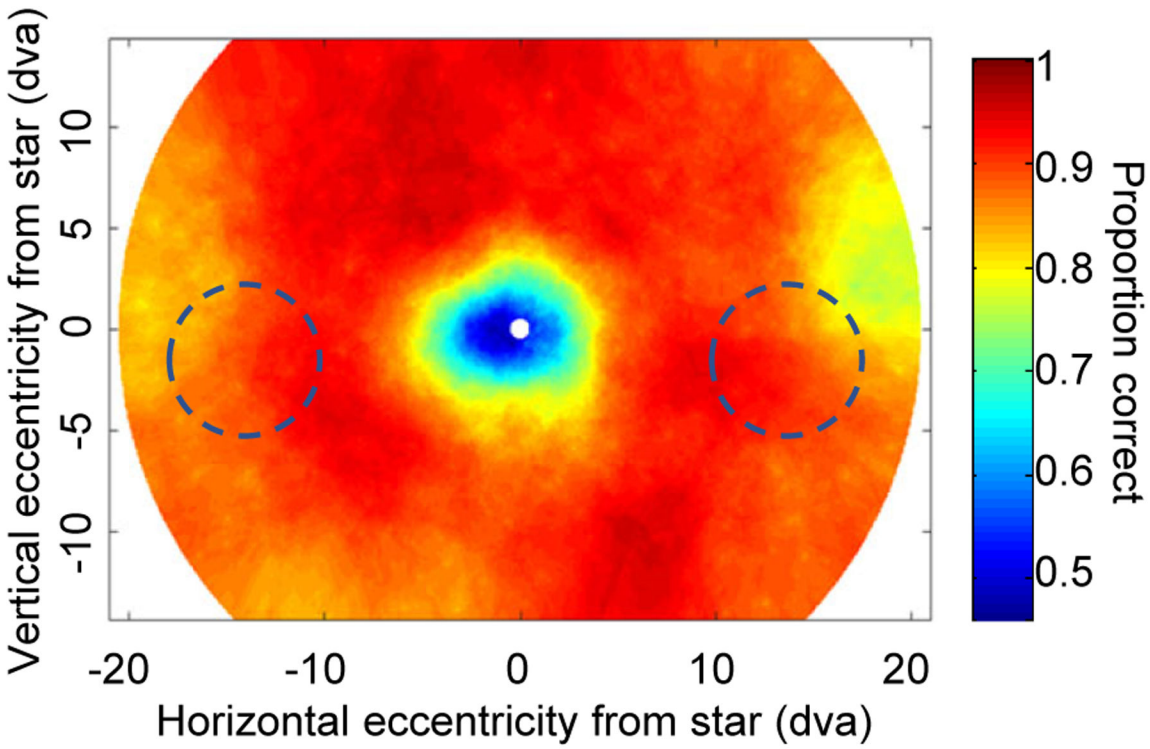

Figure 4.

Accuracy heatmap. Detection performance is indicated as a function of gaze distance from the star. Detection accuracy was at chance levels in the star's immediate vicinity and increased steeply with distance in all directions. Accuracy started to decrease once again after ~14° of eccentricity (tested in Experiment 1 along the horizontal axis only). Star locations estimated as falling on the optic discs of either eye (dashed circles) did not result in lower performance than in other equidistant locations. N=12 participants.

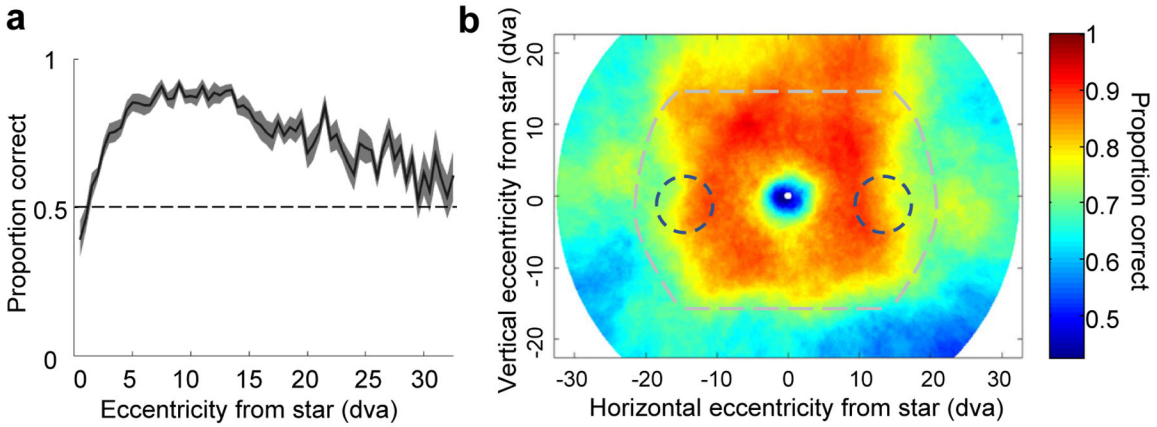

Figure 5.

(a) Detection accuracy in a greater range of horizontal and vertical eccentricities, and with a dimmer star. Consistent with Experiment 1's results, accuracy was characterized by chance levels of performance at the fovea, followed by a steep increase in performance peaking at ~8°. Around 15°, performance began to decline, further decreasing at distances past 20.5°, which Experiment 2 tested for the first time. Chance levels of performance, indicated by the dashed horizontal line, were approached at ~30°. Shading indicates SE. **(b)** The accuracy heatmap from the data in **(a)** further illustrates chance performance at the fovea, followed by peak accuracy at ~8°, and decreased performance after ~15°. The larger range of eccentricities tested in Experiment 2 showcases that the decrease in accuracy with eccentricity occurs not only in the horizontal, but also along the vertical axis, especially when foveating the upper part of the display. The black dashed circles indicate the optic discs of either eye, and the gray dashed shape designates the more limited range of Experiment 1's display. We note that performance within this region should be similar, but not necessarily identical to that in Experiment 1, given that the star stimuli had different brightness values in the two experiments. N = 14 participants.

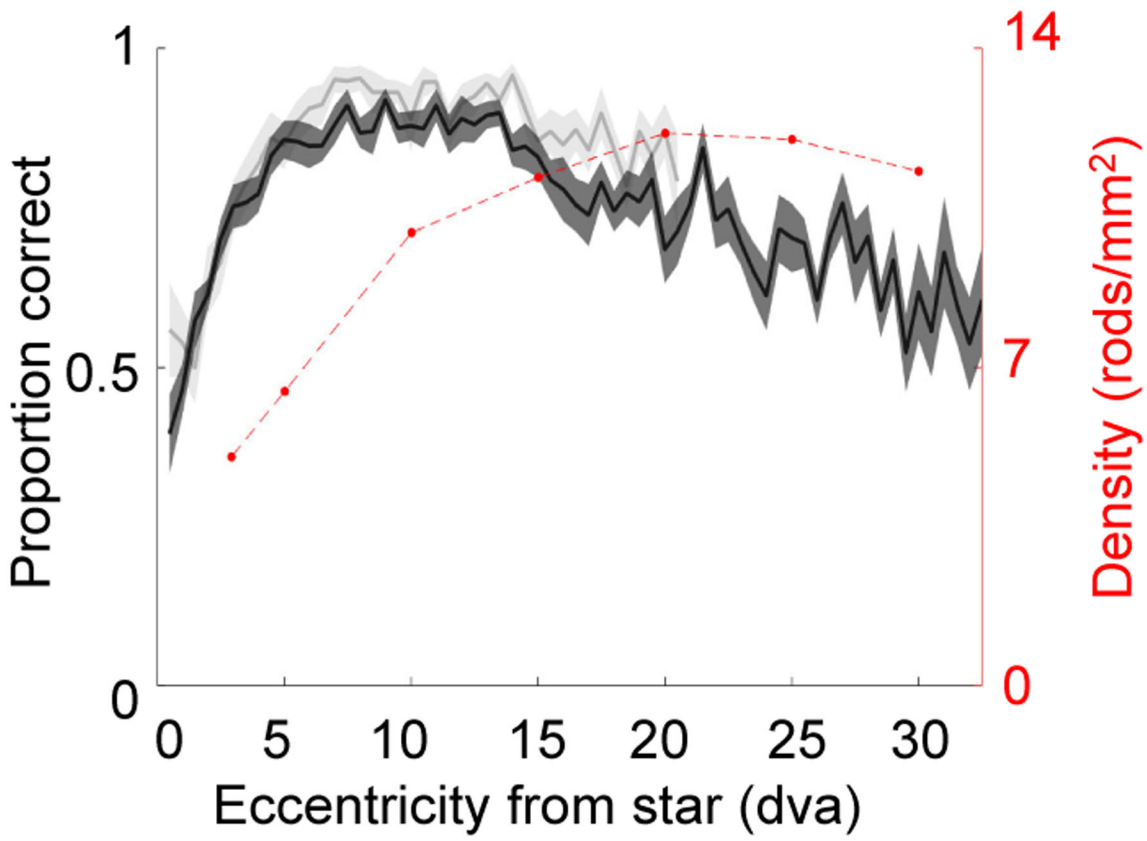

Figure 6.

Detection accuracy from Experiment 1 (gray line; N = 12) and Experiment 2 (black line; N = 14) plotted together for comparison. Peak performance for both experiments occurred in the 8°–14° range. The red-dashed curve represents the known rod density in humans (data from (Wells-Gray, Choi, Bries, & Doble, 2016)), which does not resemble the pattern of results obtained from either experiment in the current study. We note that, though the plotted rod density data has been averaged across the nasal and temporal directions, peak rod density is also found at 20°–25° in either direction before averaging. Shading on the black and gray lines indicates SE.